Extended amygdala-parabrachial circuits alter threat assessment to regulate feeding

Authors: Dionnet L. Bhatti[1,2,11][*], Andrew T. Luskin[1,2,4,6,7,8][*], Christian E. Pedersen[1,2,3,6,7,9], Bernard Mulvey[4,5], Hannah Oden-Brunson[1,2], Kate Kimbell[1,2], Abbie Sawyer[10], Robert W. Gereau IV[1,2,4], Joseph D. Dougherty[4,5], Michael R. Bruchas[1,2,3,4,6,7,8,9,12#]

Affiliations:

1 Department of Anesthesiology, Washington University School of Medicine, St. Louis, MO 63108, USA

2 Washington University Pain Center, Washington University School of Medicine, St. Louis, MO 63108, USA

3 Department of Biomedical Engineering, Washington University School of Medicine, St. Louis, MO, 63108 USA

4 Division of Biology and Biomedical Sciences, Washington University School of Medicine, St. Louis, MO, USA.

5 Department of Genetics, Washington University School of Medicine, St. Louis, MO, USA.

6 Department of Anesthesiology and Pain Medicine, University of Washington, Seattle, WA, USA

7 Center for Neurobiology of Addiction, Pain, and Emotion, University of Washington, Seattle, WA, USA

8 Graduate Program in Neuroscience, University of Washington, Seattle, WA, 98195

9 Department of Bioengineering, University of Washington, Seattle, WA, 98195

10 Department of Electrical Engineering, University of Washington, Seattle, WA, 98195

11 Current address: Program in Neuroscience, Harvard Medical School, Boston, MA 02115

12 Lead Contact

26   #Corresponding author. Email: mbruchas@uw.edu (M.R.B.)

27   *these authors contributed equally

28

29   **Abstract:**

30   An animal's evolutionary success depends on the ability to seek and consume foods while

31   avoiding environmental threats. However, how evolutionarily conserved threat detection circuits

32   modulate feeding is unknown. In mammals, feeding and threat assessment are strongly

33   influenced by the parabrachial nucleus (PBN), a structure that responds to threats and inhibits

34   feeding. Here, we report that the PBN receives dense inputs from the bed nucleus of the stria

35   terminalis (BNST), an extended amygdala structure that encodes affective information. Using a

36   series of complementary approaches, we identify opposing BNST-PBN circuits that modulate a

37   genetically-defined population of PBN neurons to control feeding. This previously unrecognized

38   neural circuit integrates threat assessment with the intrinsic drive to eat.

39

42 **Main text:**

43

44 **Introduction**

45 　　　All animals must successfully seek and consume food while avoiding environmental

46 threats to survive. The internal state of an animal directly impacts the expression of risky

47 behaviors, such as exploring a dangerous environment to obtain rewards and maintain

48 homeostasis. Animals must adaptively prioritize certain behaviors to appropriately respond to their

49 internal state (Alhadeff et al., 2018; Burnett et al., 2016). While many studies have explored the

50 interaction of metabolic need states with behavior, how mammals integrate affective-threat

51 assessment with internal need states remains largely unknown.

52 　　　Several recent reports have found that in mammals, food consumption and threat

53 assessment are heavily influenced by the parabrachial nucleus (PBN), a pontine structure that

54 integrates visceral and sensory information to encode metabolic needs (Campos et al., 2016,

55 2018; Carter et al., 2013; Essner et al., 2017; Han et al., 2015; Mu et al., 2017; Roman et al.,

56 2016; Ryan et al., 2017; Zséli et al., 2016). The amygdala and extended amygdala are

57 evolutionarily conserved brain regions that encode and integrate valence, stress, and threat to

58 alter behavioral states. Anatomical data suggest that the PBN receives input from several regions

59 that may encode affective information, including the bed nucleus of the stria terminalis (BNST), a

60 structure in the extended amygdala (Douglass et al., 2017; Kim et al., 2013; Mazzone et al., 2018;

61 Zséli et al., 2016). However, the neural circuit mechanisms that underlie the integration of an

62 animal's own motivation to eat with internal affective states regarding environmental threats are

63 still unknown. Here, we identified two previously unknown afferents from distinct populations

64 within the BNST to the PBN that underlie the complex integration of threat-assessment and

65 feeding signals to modulate PBN activity and ultimately regulate state-dependent feeding.

66

67

68   **Results**

69   **Anatomical and Molecular Characterization of Opposing BNST-PBN Circuits**

70   The BNST is a heterogeneous population comprised of glutamatergic, GABAergic, and

71   peptidergic neurons (Daniel and Rainnie, 2016; Giardino et al., 2018; Gungor and Paré, 2016;

72   Gungor et al., 2018; Jennings et al., 2013a, 2013b). To determine whether distinct neuronal

73   circuits from the BNST innervate the PBN to alter feeding behaviors, we injected Cre-inducible

74   anterograde AAVs expressing channelrhodopsin-2 with an eYFP reporter (AAV5-DIO-ChR2-

75   eYFP) into the BNST of vesicular GABA transporter (vGAT)-Cre and vesicular glutamate

76   transporter (vGLUT2)-Cre mice, which revealed robust axonal projections to the PBN from

77   GABAergic (**Figures 1A and S1F-S1K**) and glutamatergic (**Figure 1D**) BNST neurons. To further

78   substantiate our anterograde tracing findings, we used Cre-inducible retrograde adeno-

79   associated viruses (retro-AAV2) expressing an enhanced yellow fluorescent protein (eYFP)

80   reporter (AAV2retro-DIO-eYFP) (Tervo et al., 2016) into the PBN of vGAT-Cre or vGLUT2-Cre

81   mice (**Figure S1A**). Retrograde tracing revealed populations of both GABAergic and

82   glutamatergic BNST neurons that innervate the PBN (**Figure S1A**).

83   We next assessed whether these distinct populations make functional monosynaptic

84   connections to PBN neurons using *ex vivo* patch-clamp electrophysiology. We collected acute

85   brain slices containing the PBN from either vGAT-Cre or vGLUT2-Cre mice expressing DIO-

86   ChR2-eYFP in BNST-PBN projections. We optogenetically evoked post-synaptic currents in PBN

87   neurons receiving BNST GABAergic (**Figure 1B**) or glutamatergic (**Figure 1E**) innervation during

88   whole-cell patch clamp recording. Optogenetic activation of GABAergic BNST terminals in the

89   PBN evoked IPSCs that were pharmacologically blocked using GABA$_A$ antagonists (**Figure 1C**),

90   while optogenetic activation of glutamatergic BNST terminals in the PBN evoked EPSCs that were

91   pharmacologically blocked using AMPAR/NMDAR antagonists (**Figure 1F**). Postsynaptic

92   currents occurred <5ms after the light pulse, suggesting that both excitatory and inhibitory

93   connections are monosynaptic (**Figure S1B-E**).

94   We further characterized the molecular expression profiles of these distinct inhibitory and

95   excitatory BNST-PBN projections by using translating ribosome affinity purification (TRAP) to

96   determine their translational signature (Doyle et al., 2008). We generated a new Cre-dependent

97   TRAP construct within the retro-AAV2 vector (AAV2retro-DIO-TRAP) and injected it into the PBN

98   of vGAT-Cre and vGLUT2-Cre mice to isolate RNA transcripts from each BNST-PBN projection

99   population with genotype and projection specificity (Parker et al., 2019; Tervo et al., 2016). We

100   then isolated and sequenced ribosome-bound mRNA from the BNST in each group (**Figures 1G,**

101   **S2A, and S2B**). The vGAT and vGLUT2 projections are enriched in several genes of interest

102   (**Figures 1H, 1I, and S2C-S2E**). BNST-PBN^{vGAT} neurons are enriched in the neuropeptide

103   mRNAs *tachykinin 2* (*Tac2*) (Zelikowsky et al., 2018) and *galanin* (*Gal*), as well as a somatostatin

104   receptor (*Sstr3*) and *melanocortin-2 receptor accessory protein 2* (*Mrap2*), which play important

105   roles in limiting anxiety, responses and regulating feeding behavior (Ahrens et al., 2018; Asai et

106   al., 2013; Bruschetta et al., 2018; Elsilä et al., 2018). BNST-PBN^{vGLUT2} neurons are enriched in

107   *Adcyap1*, which encodes the neuropeptide PACAP, previously identified as a major regulator of

108   stress responses in the BNST (Hammack et al., 2009; Roman et al., 2014), including in contexts

109   of addiction and post-traumatic stress disorder (Miles et al., 2018; Ressler et al., 2011). Both

110   BNST-PBN^{vGAT} and BNST-PBN^{vGLUT2} neurons express calcitonin receptor *(Calcr),* recently

111   associated with the regulation of feeding (Cheng et al., 2020; Pan et al., 2018), and *nociceptin*

112   *(Pnoc*), linked to motivated behaviors including feeding (Hardaway et al., 2019; Parker et al.,

113   2019; Toll et al., 2016). We further validated these RNAseq findings by performing fluorescent in-

114   situ hybridization experiments, which revelaed co-expression of *Tac2*, *Sstr3*, and *Calcr* with

115   vGAT and *Adcyap1* with vGLUT2 neurons within the BNST (**Figures S2F-S2I**).

116

117   **Feeding and Threat Differentially Engage Excitatory and Inhibitory BNST-PBN Circuits**

118   To determine whether these distinct genetically-defined BNST-PBN circuits modulate

119   feeding behavior, we used fiber photometry to monitor calcium-mediated fluorescence, a proxy

120   for neuronal activity, of BNST-PBN terminals in freely-behaving mice (Gunaydin et al., 2014;

121   Pologruto et al., 2004). To determine whether GABAergic BNST-PBN terminals are engaged

122   during feeding behavior, we targeted AAVDJ-DIO-GCaMP6s to the BNST of vGAT-Cre mice and

123   positioned optical fibers above the PBN for measurement of BNST-PBN GABAergic terminal

124   calcium activity (**Figures 2A, 2B, and S3A, S3C, and S3E**). We found that BNST-PBN^{vGAT}

125   GCaMP activity increased as an animal engaged in both sated and hedonic feeding (i.e. sucrose),

126   as well as in other food seeking modalities including high-fat, food deprived, and normal chow

127   within novel-anxiogenic environments (**Figures 2C-2K and S3G**). Conversely, to assess whether

128   glutamatergic input to the PBN is altered during feeding behavior, we targeted AAVDJ-DIO-

129   GCaMP6s to the BNST of vGLUT2-Cre mice and similarly positioned optical fibers above the PBN

130   for measurement of BNST-PBN glutamatergic terminal calcium activity (**Figures 3A, 3B, and**

131   **S3B, S3D, and S3F**). In these experiments, we found that BNST-PBN^{vGLUT2} GCaMP activity

132   decreased when an animal engaged in these same feeding behaviors (**Figures 3C-3K**). Together,

133   these data suggest a differential opposing role for GABAergic and glutamatergic BNST-PBN

134   circuits in modulating feeding behavior.

135   Food-seeking requires an alteration of threat assessment and anxiety-like behavior in

136   order to adaptively seek out and consume food as necessary for survival. We therefore

137   hypothesized that if these circuits indeed alter feeding behavior concurrently with threat

138   assessment, GABAergic or glutamatergic BNST-PBN input may be differentially engaged during

139   aversive threat stimuli, respectively. To assess this, we recorded from BNST-PBN terminals in

140   vGAT-Cre and vGLUT-Cre mice during the presentation of multiple shock stimuli (**Figure 4A)**.

141   When animals were presented with an aversive shock, BNST-PBN^{vGAT} calcium transient activity

142   rapidly decreased in response (**Figures 4B-4D)**, while BNST-PBN^{vGLUT2} activity increased

143   following shock (**Figures 4E-4F**). These observations indicate that inhibitory GABAergic BNST-

144   PBN circuits may act to diminish threat signaling to engage and allow feeding, while excitatory

145   glutamatergic BNST-PBN circuits could be recruited to enhance threat signaling and suppress

146   feeding behaviors.

147

148   **Excitatory and Inhibitory BNST-PBN Circuit Activation Drive Opposing Feeding Behavior**

149   Since photometry measurements at the terminals revealed that these two opposing BNST-

150   PBN projections are modulated during feeding and threat responses, we next utilized optogenetic

151   approaches to assess whether manipulating neural circuit activity of BNST-PBN circuits alters

152   feeding, threat, and affective valence, and to determine direct causality of this circuit in regulating

153   behavior. We targeted AAV5-EF1α-DIO-ChR2 to the BNST of vGAT-Cre or vGLUT2-Cre mice

154   and positioned optical fibers above the PBN for photo-stimulation of BNST-PBN GABAergic or

155   glutamatergic terminals (**Figure 5A**). First, we measured food consumption with or without

156   genetically defined neural circuit photo-activation while mice had free access to different foods

157   (**Figure 5B**). Activation of ChR2 in BNST-PBN^{vGAT} neurons increased food consumption

158   compared to control mice under sated conditions (**Figure 5C and S4B**). This increase also

159   occurred with sucrose and high-fat foods (**Figures S4D-S4F**). Furthermore, photoactivation of

160   BNST-PBN^{vGAT} signaling also increased consumption of less-palatable salt-enriched or bitter (i.e.

161   quinine-enriched) foods (**Figure S4G-S4I**). Notably, this BNST-PBN^{vGAT}-mediated increase in

162   feeding was present when the animal was sated but was not evident after food deprivation (**Figure**

163   **5C, Figure S4C**). Together, these results suggest that the inhibitory BNST-PBN circuit is sufficient

164   to drive feeding in sated states, regardless of food type, and likely overrides the valence of the

165   food. In contrast, we saw a ceiling effect in the food-deprived state, suggesting that inhibitory

166   BNST-PBN circuits are already engaged, consistent with our fiber photometry data (**Figure S3G)**.

167   Additionally, optogenetic inhibition of the BNST-PBN^{vGAT} circuit using Arch3.0 revealed its

168   necessity for hunger-driven feeding (**Figures S4P-S4R**). In contrast to activation of BNST-

169   PBN^{vGAT}, activation of BNST-PBN^{vGLUT2} circuits in a food-deprived state decreased consumption

170   of normal chow (**Figures 5D and S5A-S5E)**, demonstrating that the excitatory BNST-PBN circuit

171   is sufficient to reduce feeding when mice in a food-deprived state, suggesting binary and opposing

172   BNST-PBN circuits.

173

174   **Excitatory and Inhibitory BNST-PBN Circuit Activation Drive Opposing Affective States**

175   Internal state (affective valence) alters an animal's ability to assess potential threats and

176   explore different environments, a requirement to locate and consume foods. Therefore, we sought

177   to assess the affective valence of these distinct BNST-PBN circuits by subjecting mice to real-

178   time-place-preference (RTPP) tests and operant-reinforcement assays (Al-Hasani et al., 2015;

179   McCall et al., 2015; Seo et al., 2016). We injected AAV5-EF1α-DIO-ChR2 into the BNST of vGAT-

180   Cre or vGLUT2-Cre mice, placing an optic fiber above the PBN, and tested whether stimulation

181   of this BNST-PBN^{vGAT} pathway was reinforcing or aversive. In the RTPP assay, photoactivation

182   of ChR2 in BNST-PBN^{vGAT} neurons resulted in a robust place preference for the photostimulation-

183   paired side, while photoactivation of ChR2 in BNST-PBN^{vGLUT2} neurons resulted in a robust place

184   aversion for the photostimulation-paired side, as compared to controls (**Figures 5E and 5F**). In

185   an operant self-stimulation paradigm, photoactivation of BNST-PBN^{vGAT} neurons significantly

186   increased the number of nosepokes for self-stimulation relative to controls (**Figure 5H**),

187   demonstrating that BNST-PBN^{vGAT} stimulation is positively reinforcing. Conversely,

188   photoactivation of BNST-PBN^{vGLUT2} neurons significantly increased the number of nosepokes

189   mice performed to turn off photostimulation (**Figures 5I and S5F**), demonstrating that BNST-

190   PBN^{vGLUT2} stimulation is negatively reinforcing. These data indicate that activation of GABAergic

191   and glutamatergic BNST-PBN circuits have innate positive and negative affective valence,

192   respectively (Namburi et al., 2016).

193   To assess whether BNST-PBN circuits modulate threat-assessment, we tested mice in

194   the elevated zero maze (EZM), which measures anxiety-like behaviors and exploration in a novel

195   brightly lit anxiogenic context (McCall et al., 2015). When EZM experiments were conducted in a

196   brightly lit aversive setting, mice with photoactivation of BNST-PBN^{vGAT} neurons spent more time

197   in the open arms compared to controls (**Figures 5J, S4K, and S4L**), consistent with increased

198   exploratory drive. In contrast, mice with photoactivation of BNST-PBN^{vGLUT2} neurons showed

199   decreased exploration of the open arms (**Figure 5K**), indicating that stimulation of this circuit is

200   sufficient to reduce exploration of an anxiogenic environment. As a further test of whether BNST-

201   PBN^{vGAT} activation can suppress defensive behaviors associated with threat, we subjected mice

202   to threat-conditioning and measured their defensive response (freezing) to a conditioned stimulus.

203   Mice were trained to associate a conditioned stimulus (tone) with a highly aversive unconditioned

204   stimulus (0.7 mA, 2-s footshock). Photostimulation of BNST-PBN^{vGAT} neurons robustly reduced

205   the defensive responses to the conditioned stimulus (**Figures 5L and 5M**). These data indicate

206   that BNST-PBN circuits are sufficient and necessary for regulating opposing behavioral states

207   including anxiety and threat within the context of feeding behavior.

208

209   **pDyn-expressing PBN neurons receive BNST input and alter feeding and affective behavior**

210   We next aimed to determine the specific targets of BNST^{vGAT} and BNST^{vGLUT2} projections

211   in the PBN. Previous studies have identified diverse neuronal populations within the primarily

212   glutamatergic PBN (Carter et al., 2013; Geerling et al., 2015; Miller et al., 2011; Ryan et al., 2017).

213   Here we examined dynorphin (pDyn) neurons, previously shown to regulate thermoregulation

214   (Cintron-Colon et al., 2019; Geerling et al., 2015), and CGRP neurons (Campos et al., 2016;

215   Carter et al., 2013; Han et al., 2015), shown to function as a general alarm system that responds

216   to threats and inhibits feeding when activated. In-situ hybridization experiments demonstrated

217   that pDyn neurons and CGRP neurons form genetically and anatomically distinct populations in

218   the PBN (**Figures 6A and 6B**). Using a transsynaptic rabies tracing method (Beier et al., 2015;

219   Schwarz et al., 2015; Wickersham et al., 2007), we found that BNST neurons indeed form

220   monosynaptic connections with pDyn-expressing neurons in the PBN (**Figures 6C-6E**) and may

221   therefore be a critical downstream node for the behavioral effects of inhibitory and excitatory

222   BNST-PBN inputs.

223   We targeted dynorphin-expressing PBN neurons in pDyn-Cre mice with AAV5-EF1α-DIO-

224   ChR2 and subjected the mice to a both feeding and affective behavioral tests (**Figures 6F and**

225   **6G**). Consistent with the effects of excitatory BNST-PBN activation, we found that

226   photostimulation of PBN^{pDyn} produces a robust real-time place aversion (**Figures 6H-6J, S6A,**

227   **and S6B**) and reduced feeding when animals were in a food-deprived state (**Figures 6K and**

228   **S6C**). Additionally, inhibition of the broader PBN^{vGLUT2} population rapidly and reversibly increased

229   food consumption (**Figures S6D and S6E)**. Likewise, chemogenetic inhibition of PBN^{pDyn} neurons

230   using the hM4Di DREADD strategy (Armbruster et al., 2007) decreased the latency to consume

231   food in an anxiogenic environment and increased overall food consumption in mice expressing

232   the inhibitory DREADD when given CNO compared to saline, while control animals did not differ

233   between treatments (**Figure 6L-6P**). Consistent with this finding, the inhibition of PBN^{pDyn} neurons

234   produced anxiolytic behavior in an EZM test (**Figure 6Q**). These data reveal a previously

235   unrecognized functional role of PBN^{pDyn} neurons as primary integrators of BNST afferents that

236   coordinate feeding drive with threat assessment.

237

238   **Discussion**

239   These studies indicate that discrete and opposing neural circuitry from the BNST to the

240   PBN integrates internal states, threat assessment, and feeding behavior. The BNST has been

241   shown to be involved in numerous functions related to threats and motivated behaviors (Lebow

242   and Chen, 2016), and our findings demonstrate that the BNST conveys sensory and affective

243   information to the PBN to alter behavior critical to an animal's survival.

244   Recent studies have demonstrated BNST input to the PBN and revealed that BNST

245   neurons may influence respiration and anxiety via increased metabolic activity in the parabrachial

246   nucleus (Kim et al., 2013; Mazzone et al., 2018). Nonetheless, studies to date had not determined

247   the identity of these projections. Employing the use of genetic targeting in our study, we unveil a

248   separable role for discrete genetically-defined BNST-PBN projections. We also identify the

249   complement of mRNAs actively translated by PBN-projecting BNST neurons in a cell-type specific

250   manner, revealing several peptides and receptors that may act as neuromodulatory regulators

251   influencing affect and feeding (**Figures 1G-1I**). Notably, these peptides and receptors provide an

252   entryway to follow up studies and the development of new therapeutic strategies for treating

253   feeding and affective diseases including obesity, generalized anxiety, and depression. Future

254   studies employing Cre driver lines and pharmacological approaches will be critical to dissect the

255   neuropeptide and receptor systems influencing these complex anxiety-like and feeding behaviors.

256   In this study, we also probe the neural dynamics and functional roles of opposing BNST-

257   PBN circuits using fiber photometry together with optogenetics. Our results reveal that the

258   GABAergic BNST-PBN circuit is engaged by and drives feeding behavior and exploration, while

259   the glutamatergic BNST-PBN circuit is disengaged during feeding and suppresses state-

260   dependent feeding and exploration (**Figures 2-5**). Interestingly, the distinct circuits begin

261   increasing or decreasing their activity prior to the consumption itself, suggesting that the circuit is

262   not only encoding the consumption but the appetitive behavior as well. Furthermore, we

263   demonstrate that these opposing inhibitory and excitatory circuits act to drive these behaviors

264   partly via the attribution of valence inherent to the circuit itself (**Figure 5**). Further studies exploring

265   both acute and learned threat detection with opposing feeding states will be needed to explore

266   how these circuits adapt under various environmental influences. Here we demonstrate that

267   activation of these circuits is sufficient to alter feeding, exploration, and threat assessment. Given

268   that eating disorders are highly associated with varying affective states (Hardaway et al., 2015),

269   further investigation of these circuits under varying affective states imposed by external adverse

270   experiences such as pain or stress is necessary to fully understand the extent of their involvement.

271   The PBN consists of many cell-types that may mediate separable aspects of feeding and

272   aversion (Campos et al., 2018; Fu et al., 2019; Park et al., 2020; Ryan et al., 2017). Of these cell-

273   types, neurons expressing calcitonin gene-related peptide (CGRP) located in the vental/external

274   lateral parabrachial (PBNel) thought to function as a general alarm system that sends aversive

275 signals throughout the brain are of the most notable (Palmiter, 2018). However, our results

276 demonstrate that GABAergic and glutamatergic BNST terminals are most dense in the

277 dorsolateral and medial regions of the PBN and lacking in the ventrolateral region where CGRP

278 neurons subside (**Figures 1A, 1D, 6A, 6B, and S1A**). This was both interesting and surprising to

279 us because this reveals that although CGRP neurons mediate feeding and aversion, they are not

280 the sole neuropeptide population in the PBN mediating these behaviors. In our studies, we have

281 demonstrated that dynorphin-expressing neurons located in the dorsolateral PBN (PBN^{pDyn}) are

282 also critically poised as functional mediators of feeding and affective behaviors (Bhatti et al.,

283 2018). Additionally, recent studies seem to suggest that PBN^{pDyn} may communicate with CGRP

284 neurons in response to noxious pain stimuli (Chiang et al., 2019). Prior to this study, the primary

285 function for PBN^{pDyn} was thought to be for thermoregulation (Cintron-Colon et al., 2019; Geerling

286 et al., 2015). Altogether, these studies with our results suggest that a primary role for PBN^{pDyn} is

287 to integrate internal states including threat assessment, anxiety, thermoregulation, or pain, in

288 order to adaptively seek and consume or avoid food.

289   Here we present two opposing neural circuits from the BNST to the PBN that mediate

290 threat-assessment, exploration, and feeding behaviors in part via their connections to dynorphin-

291 expressing PBN neurons. Our results implicate these circuits, neuropeptide candidates, and both

292 inhibitory and excitatory BNST neurons as critical integrators with the PBN for adaptive and

293 affective behaviors necessary for survival. These findings may provide new avenues for the

294 development of unique strategies to mitigate maladaptive behaviors related to eating patterns or

295 affective state.

296

297

298

299 **References:**

300 Ahrens, S., Wu, M.V., Furlan, A., Hwang, G.-R., Paik, R., Li, H., Penzo, M.A., Tollkuhn, J., and
301 Li, B. (2018). A Central Extended Amygdala Circuit That Modulates Anxiety. J. Neurosci. *38*,
302 5567–5583.

303 Alhadeff, A.L., Su, Z., Hernandez, E., Klima, M.L., Phillips, S.Z., Holland, R.A., Guo, C.,
304 Hantman, A.W., De Jonghe, B.C., and Betley, J.N. (2018). A Neural Circuit for the Suppression
305 of Pain by a Competing Need State. Cell *173*, 140-152.e15.

306 Al-Hasani, R., McCall, J.G., Shin, G., Gomez, A.M., Schmitz, G.P., Bernardi, J.M., Pyo, C.-O.,
307 Park, S.I., Marcinkiewcz, C.M., Crowley, N.A., et al. (2015). Distinct Subpopulations of Nucleus
308 Accumbens Dynorphin Neurons Drive Aversion and Reward. Neuron *87*, 1063–1077.

309 Armbruster, B.N., Li, X., Pausch, M.H., Herlitze, S., and Roth, B.L. (2007). Evolving the lock to
310 fit the key to create a family of G protein-coupled receptors potently activated by an inert ligand.
311 Proc Natl Acad Sci U S A *104*, 5163–5168.

312 Asai, M., Ramachandrappa, S., Joachim, M., Shen, Y., Zhang, R., Nuthalapati, N.,
313 Ramanathan, V., Strochlic, D.E., Ferket, P., Linhart, K., et al. (2013). Loss of Function of the
314 Melanocortin 2 Receptor Accessory Protein 2 Is Associated with Mammalian Obesity. Science
315 *341*, 275–278.

316 Beier, K.T., Steinberg, E.E., DeLoach, K.E., Xie, S., Miyamichi, K., Schwarz, L., Gao, X.J.,
317 Kremer, E.J., Malenka, R.C., and Luo, L. (2015). Circuit Architecture of VTA Dopamine Neurons
318 Revealed by Systematic Input-Output Mapping. Cell *162*, 622–634.

319 Bhatti, D.L., Luskin, A.T., Pedersen, C.E., Kimbell, K., Oden-Brunson, H., Gereau, R.W., and
320 Bruchas, M.R. (2018). Extended amygdala-parabrachial circuits alter threat perception and
321 encode homeostatic and hedonic feeding (Society for Neuroscience, San Diego, CA).

322 Bruschetta, G., Kim, J.D., Diano, S., and Chan, L.F. (2018). Overexpression of melanocortin 2
323 receptor accessory protein 2 (MRAP2) in adult paraventricular MC4R neurons regulates energy
324 intake and expenditure. Molecular Metabolism *18*, 79–87.

325 Burnett, C.J., Li, C., Webber, E., Tsaousidou, E., Xue, S.Y., Brüning, J.C., and Krashes, M.J.
326 (2016). Hunger-Driven Motivational State Competition. Neuron *92*, 187–201.

327 Campos, C.A., Bowen, A.J., Schwartz, M.W., and Palmiter, R.D. (2016). Parabrachial CGRP
328 Neurons Control Meal Termination. Cell Metabolism *23*, 811–820.

329 Campos, C.A., Bowen, A.J., Roman, C.W., and Palmiter, R.D. (2018). Encoding of danger by
330 parabrachial CGRP neurons. Nature *555*, 617–622.

331 Carter, M.E., Soden, M.E., Zweifel, L.S., and Palmiter, R.D. (2013). Genetic identification of a
332 neural circuit that suppresses appetite. Nature *503*, 111–114.

333 Cheng, W., Gonzalez, I., Pan, W., Tsang, A.H., Adams, J., Ndoka, E., Gordian, D., Khoury, B.,
334 Roelofs, K., Evers, S.S., et al. (2020). Calcitonin Receptor Neurons in the Mouse Nucleus
335 Tractus Solitarius Control Energy Balance via the Non-aversive Suppression of Feeding. Cell
336 Metabolism.

337   Chiang, M.C., Nguyen, E.K., Papale, A.E., and Ross, S.E. (2019). Divergent neural pathways
338   emanating from the lateral parabrachial nucleus mediate distinct components of the pain
339   response. BioRxiv 602466.

340   Cintron-Colon, R., Johnson, C.W., Montenegro-Burke, J.R., Guijas, C., Faulhaber, L., Sanchez-
341   Alavez, M., Aguirre, C.A., Shankar, K., Singh, M., Galmozzi, A., et al. (2019). Activation of
342   Kappa Opioid Receptor Regulates the Hypothermic Response to Calorie Restriction and Limits
343   Body Weight Loss. Current Biology *29*, 4291-4299.e4.

344   Daniel, S.E., and Rainnie, D.G. (2016). Stress Modulation of Opposing Circuits in the Bed
345   Nucleus of the Stria Terminalis. Neuropsychopharmacology *41*, 103–125.

346   Douglass, A.M., Kucukdereli, H., Ponserre, M., Markovic, M., Gründemann, J., Strobel, C.,
347   Morales, P.L.A., Conzelmann, K.-K., Lüthi, A., and Klein, R. (2017). Central amygdala circuits
348   modulate food consumption through a positive-valence mechanism. Nature Neuroscience *20*,
349   1384–1394.

350   Doyle, J.P., Dougherty, J.D., Heiman, M., Schmidt, E.F., Stevens, T.R., Ma, G., Bupp, S.,
351   Shrestha, P., Shah, R.D., Doughty, M.L., et al. (2008). Application of a Translational Profiling
352   Approach for the Comparative Analysis of CNS Cell Types. Cell *135*, 749–762.

353   Elsilä, L., De Miguel, E., and Korpi, E.R. (2018). P.2.036 - Somatostatin-expressing neurons in
354   the bed nucleus of stria terminalis in anxiety- and addiction-related behaviours in mice.
355   European Neuropsychopharmacology *28*, S49.

356   Essner, R.A., Smith, A.G., Jamnik, A.A., Ryba, A.R., Trutner, Z.D., and Carter, M.E. (2017).
357   AgRP Neurons Can Increase Food Intake during Conditions of Appetite Suppression and Inhibit
358   Anorexigenic Parabrachial Neurons. J. Neurosci. *37*, 8678–8687.

359   Fu, O., Iwai, Y., Kondoh, K., Misaka, T., Minokoshi, Y., and Nakajima, K. (2019). SatB2-
360   Expressing Neurons in the Parabrachial Nucleus Encode Sweet Taste. Cell Reports *27*, 1650-
361   1656.e4.

362   Geerling, J.C., Kim, M., Mahoney, C.E., Abbott, S.B.G., Agostinelli, L.J., Garfield, A.S., Krashes,
363   M.J., Lowell, B.B., and Scammell, T.E. (2015). Genetic identity of thermosensory relay neurons
364   in the lateral parabrachial nucleus. American Journal of Physiology-Regulatory, Integrative and
365   Comparative Physiology *310*, R41–R54.

366   Giardino, W.J., Eban-Rothschild, A., Christoffel, D.J., Li, S.-B., Malenka, R.C., and Lecea, L. de
367   (2018). Parallel circuits from the bed nuclei of stria terminalis to the lateral hypothalamus drive
368   opposing emotional states. Nature Neuroscience *21*, 1084–1095.

369   Gunaydin, L.A., Grosenick, L., Finkelstein, J.C., Kauvar, I.V., Fenno, L.E., Adhikari, A., Lammel,
370   S., Mirzabekov, J.J., Airan, R.D., Zalocusky, K.A., et al. (2014). Natural Neural Projection
371   Dynamics Underlying Social Behavior. Cell *157*, 1535–1551.

372   Gungor, N.Z., and Paré, D. (2016). Functional Heterogeneity in the Bed Nucleus of the Stria
373   TerminalisFunctional Heterogeneity in the Bed Nucleus of the Stria Terminalis. J. Neurosci. *36*,
374   8038–8049.

375   Gungor, N.Z., Yamamoto, R., and Pare, D. (2018). Glutamatergic and gabaergic ventral BNST
376   neurons differ in their physiological properties and responsiveness to noradrenaline.
377   Neuropsychopharmacology *43*, 2126.

378   Hammack, S.E., Cheung, J., Rhodes, K.M., Schutz, K.C., Falls, W.A., Braas, K.M., and May, V.
379   (2009). Chronic stress increases pituitary adenylate cyclase-activating peptide (PACAP) and
380   brain-derived neurotrophic factor (BDNF) mRNA expression in the bed nucleus of the stria
381   terminalis (BNST): Roles for PACAP in anxiety-like behavior. Psychoneuroendocrinology *34*,
382   833–843.

383   Han, S., Soleiman, M.T., Soden, M.E., Zweifel, L.S., and Palmiter, R.D. (2015). Elucidating an
384   Affective Pain Circuit that Creates a Threat Memory. Cell *162*, 363–374.

385   Hardaway, J.A., Crowley, N.A., Bulik, C.M., and Kash, T.L. (2015). Integrated circuits and
386   molecular components for stress and feeding: implications for eating disorders. Genes, Brain
387   and Behavior *14*, 85–97.

388   Hardaway, J.A., Halladay, L.R., Mazzone, C.M., Pati, D., Bloodgood, D.W., Kim, M., Jensen, J.,
389   DiBerto, J.F., Boyt, K.M., Shiddapur, A., et al. (2019). Central Amygdala Prepronociceptin-
390   Expressing Neurons Mediate Palatable Food Consumption and Reward. Neuron *102*, 1037-
391   1052.e7.

392   Jennings, J.H., Sparta, D.R., Stamatakis, A.M., Ung, R.L., Pleil, K.E., Kash, T.L., and Stuber,
393   G.D. (2013a). Distinct extended amygdala circuits for divergent motivational states. Nature *496*,
394   224–228.

395   Jennings, J.H., Rizzi, G., Stamatakis, A.M., Ung, R.L., and Stuber, G.D. (2013b). The inhibitory
396   circuit architecture of the lateral hypothalamus orchestrates feeding. Science *341*, 1517–1521.

397   Kim, S.-Y., Adhikari, A., Lee, S.Y., Marshel, J.H., Kim, C.K., Mallory, C.S., Lo, M., Pak, S.,
398   Mattis, J., Lim, B.K., et al. (2013). Diverging neural pathways assemble a behavioural state from
399   separable features in anxiety. Nature *496*, 219–223.

400   Lebow, M.A., and Chen, A. (2016). Overshadowed by the amygdala: the bed nucleus of the
401   stria terminalis emerges as key to psychiatric disorders. Mol Psychiatry *21*, 450–463.

402   Mazzone, C.M., Pati, D., Michaelides, M., DiBerto, J., Fox, J.H., Tipton, G., Anderson, C., Duffy,
403   K., McKlveen, J.M., Hardaway, J.A., et al. (2018). Acute engagement of G_q-mediated signaling
404   in the bed nucleus of the stria terminalis induces anxiety-like behavior. Molecular Psychiatry *23*,
405   143–153.

406   McCall, J.G., Al-Hasani, R., Siuda, E.R., Hong, D.Y., Norris, A.J., Ford, C.P., and Bruchas, M.R.
407   (2015). CRH Engagement of the Locus Coeruleus Noradrenergic System Mediates Stress-
408   Induced Anxiety. Neuron *87*, 605–620.

409   Miles, O.W., Thrailkill, E.A., Linden, A.K., May, V., Bouton, M.E., and Hammack, S.E. (2018).
410   Pituitary Adenylate Cyclase-Activating Peptide in the Bed Nucleus of the Stria Terminalis
411   Mediates Stress-Induced Reinstatement of Cocaine Seeking in Rats. Neuropsychopharmacol.
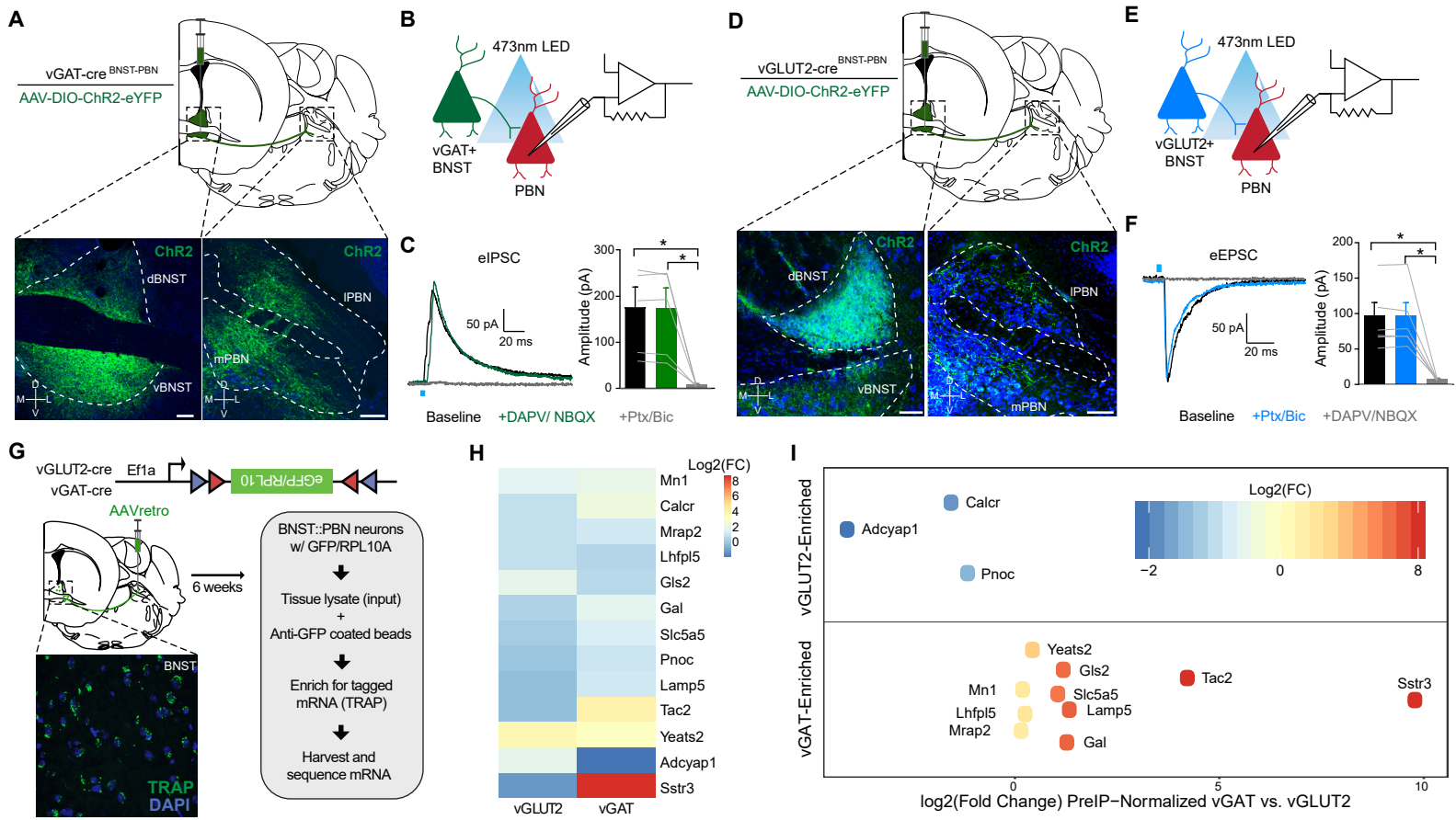412   *43*, 978–986.

413 Miller, R.L., Stein, M.K., and Loewy, A.D. (2011). Serotonergic inputs to FoxP2 neurons of the
414 pre-locus coeruleus and parabrachial nuclei that project to the ventral tegmental area.
415 Neuroscience *193*, 229–240.

416 Mu, D., Deng, J., Liu, K.-F., Wu, Z.-Y., Shi, Y.-F., Guo, W.-M., Mao, Q.-Q., Liu, X.-J., Li, H., and
417 Sun, Y.-G. (2017). A central neural circuit for itch sensation. Science *357*, 695–699.

418 Namburi, P., Al-Hasani, R., Calhoon, G.G., Bruchas, M.R., and Tye, K.M. (2016). Architectural
419 Representation of Valence in the Limbic System. Neuropsychopharmacology *41*, 1697–1715.

420 Palmiter, R.D. (2018). The Parabrachial Nucleus: CGRP Neurons Function as a General Alarm.
421 Trends in Neurosciences *41*, 280–293.

422 Pan, W., Adams, J.M., Allison, M.B., Patterson, C., Flak, J.N., Jones, J., Strohbehn, G.,
423 Trevaskis, J., Rhodes, C.J., Olson, D.P., et al. (2018). Essential Role for Hypothalamic
424 Calcitonin Receptor–Expressing Neurons in the Control of Food Intake by Leptin. Endocrinology
425 *159*, 1860–1872.

426 Park, S., Williams, K.W., Liu, C., and Sohn, J.-W. (2020). A neural basis for tonic suppression of
427 sodium appetite. Nature Neuroscience 1–10.

428 Parker, K.E., Pedersen, C.E., Gomez, A.M., Spangler, S.M., Walicki, M.C., Feng, S.Y., Stewart,
429 S.L., Otis, J.M., Al-Hasani, R., McCall, J.G., et al. (2019). A Paranigral VTA Nociceptin Circuit
430 that Constrains Motivation for Reward. Cell *178*, 653-671.e19.

431 Pologruto, T.A., Yasuda, R., and Svoboda, K. (2004). Monitoring Neural Activity and [Ca2+] with
432 Genetically Encoded Ca2+ Indicators. J. Neurosci. *24*, 9572–9579.

433 Ressler, K.J., Mercer, K.B., Bradley, B., Jovanovic, T., Mahan, A., Kerley, K., Norrholm, S.D.,
434 Kilaru, V., Smith, A.K., Myers, A.J., et al. (2011). Post-traumatic stress disorder is associated
435 with PACAP and the PAC1 receptor. Nature *470*, 492–497.

436 Roman, C.W., Lezak, K.R., Hartsock, M.J., Falls, W.A., Braas, K.M., Howard, A.B., Hammack,
437 S.E., and May, V. (2014). PAC1 receptor antagonism in the bed nucleus of the stria terminalis
438 (BNST) attenuates the endocrine and behavioral consequences of chronic stress.
439 Psychoneuroendocrinology *47*, 151–165.

440 Roman, C.W., Derkach, V.A., and Palmiter, R.D. (2016). Genetically and functionally defined
441 NTS to PBN brain circuits mediating anorexia. Nat Commun *7*, 1–11.

442 Ryan, P.J., Ross, S.I., Campos, C.A., Derkach, V.A., and Palmiter, R.D. (2017). Oxytocin-
443 receptor-expressing neurons in the parabrachial nucleus regulate fluid intake. Nature
444 Neuroscience *20*, 1722–1733.

445 Schwarz, L.A., Miyamichi, K., Gao, X.J., Beier, K.T., Weissbourd, B., DeLoach, K.E., Ren, J.,
446 Ibanes, S., Malenka, R.C., Kremer, E.J., et al. (2015). Viral-genetic tracing of the input–output
447 organization of a central noradrenaline circuit. Nature *524*, 88–92.

448 Seo, D., Funderburk, S.C., Bhatti, D.L., Motard, L.E., Newbold, D., Girven, K.S., McCall, J.G.,
449 Krashes, M., Sparta, D.R., and Bruchas, M.R. (2016). A GABAergic Projection from the

450 Centromedial Nuclei of the Amygdala to Ventromedial Prefrontal Cortex Modulates Reward
451 Behavior. J. Neurosci. *36*, 10831–10842.

452 Tervo, D.G.R., Hwang, B.-Y., Viswanathan, S., Gaj, T., Lavzin, M., Ritola, K.D., Lindo, S.,
453 Michael, S., Kuleshova, E., Ojala, D., et al. (2016). A Designer AAV Variant Permits Efficient
454 Retrograde Access to Projection Neurons. Neuron *92*, 372–382.

455 Toll, L., Bruchas, M.R., Calo', G., Cox, B.M., and Zaveri, N.T. (2016). Nociceptin/Orphanin FQ
456 Receptor Structure, Signaling, Ligands, Functions, and Interactions with Opioid Systems.
457 Pharmacol Rev *68*, 419–457.

458 Wickersham, I.R., Lyon, D.C., Barnard, R.J.O., Mori, T., Finke, S., Conzelmann, K.-K., Young,
459 J.A.T., and Callaway, E.M. (2007). Monosynaptic Restriction of Transsynaptic Tracing from
460 Single, Genetically Targeted Neurons. Neuron *53*, 639–647.

461 Zelikowsky, M., Hui, M., Karigo, T., Choe, A., Yang, B., Blanco, M.R., Beadle, K., Gradinaru, V.,
462 Deverman, B.E., and Anderson, D.J. (2018). The Neuropeptide Tac2 Controls a Distributed
463 Brain State Induced by Chronic Social Isolation Stress. Cell *173*, 1265-1279.e19.

464 Zséli, G., Vida, B., Martinez, A., Lechan, R.M., Khan, A.M., and Fekete, C. (2016). Elucidation of
465 the anatomy of a satiety network: Focus on connectivity of the parabrachial nucleus in the adult
466 rat. Journal of Comparative Neurology *524*, 2803–2827.

467

FIGURE 1

494 **Figure 1. Anatomical and molecular characterization of opposing BNST-PBN circuits.**

495 **(A)** Schematic of viral injection and representative image depicting expression in BNST^{vGAT} soma

496 and their terminals in the PBN (scale bar: 100 μm). Blue = Nissl. Green = eYFP.

497 **(B)** Schematic of whole-cell patch clamp electrophysiology recordings of optically-evoked IPSCs.

498 **(C)** Optogenetic activation of BNST^{vGAT} terminals elicit IPSCs in PBN neurons that are abolished

499 by GABA$_A$ receptor antagonism (n=5 cells, 4 mice).

500 **(D)** Schematic of viral injection and representative image depicting expression in BNST^{vGLUT2}

501 soma and their terminals in the PBN (scale bar: 100 μm). Blue = Nissl. Green = eYFP.

502 **(E)** Schematic of whole-cell patch clamp electrophysiology recordings of optically-evoked EPSCs.

503 **(F)** Optogenetic activation of BNST^{vGLUT2} terminals elicit EPSCs in PBN neurons that are

504 abolished by AMPA/NMDA receptor antagonism (n=6 cells, 5 mice).

505 (**G**) Cartoon of injection of TRAP into PBN of vGLUT2-Cre or vGAT-Cre animals. Tagged mRNA

506 was extracted from the BNST and sequenced. Inset: representative image of TRAP-GFP
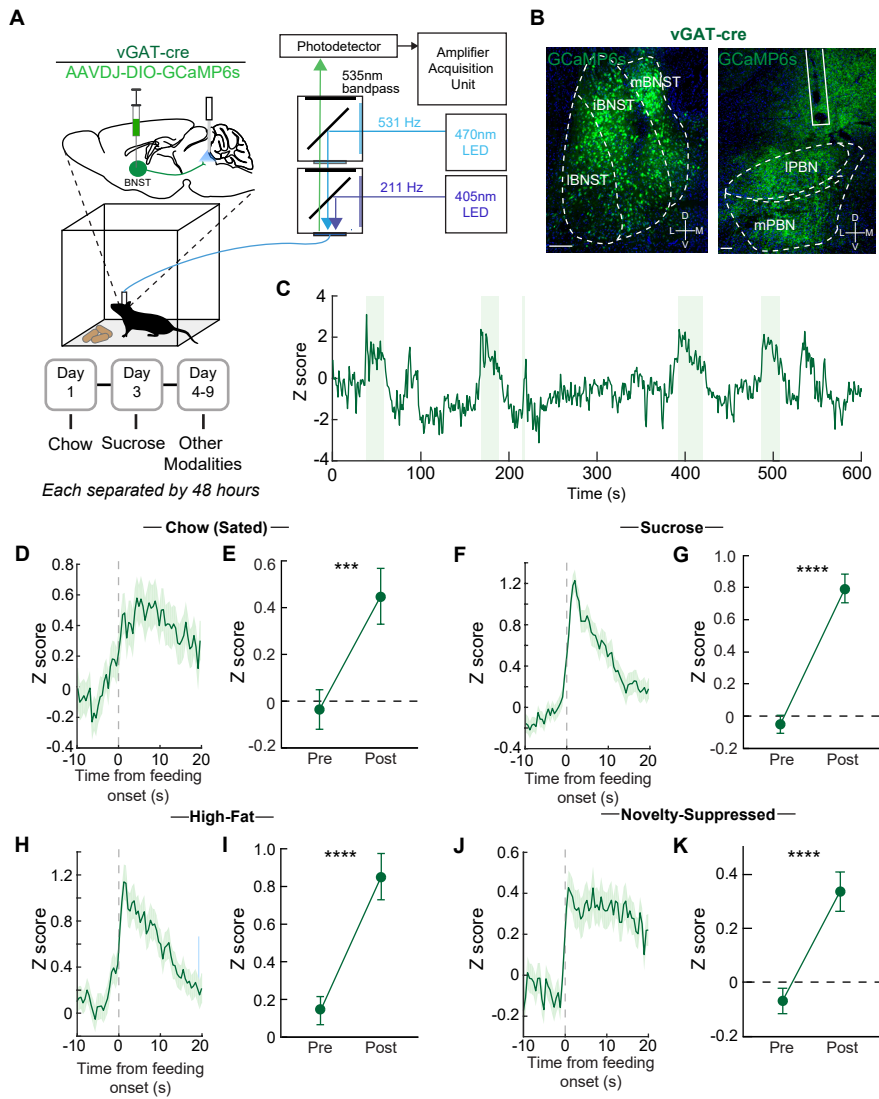
507 expression in BNST.

508 (**H**) Heatmap of transcripts enriched in either vGAT or vGLUT2 projections from BNST to PBN

509 over input homogenate (pre-IP) (n=3 vGLUT2-Cre samples; n=2 vGAT-Cre samples).

510 (**I**) Transcripts enriched in either vGAT or vGLUT2 projections from BNST to PBN, after

511 normalization to respective input (pre-IP) homogenates. Positive Log2(FC) values indicate

512 transcript enrichment in BNST-PBN^{vGAT} neurons relative to BNST-PBN^{vGLUT2} neurons;

513 negative Log2(FC) values indicate relative enrichment in BNST-PBN^{vGLUT2} neurons.

514 *p < 0.05. Error bars indicate SEM.

515 See also Figure S1 and S2.

FIGURE 2

516 **Figure 2. Feeding behavior engages an inhibitory BNST-PBN circuit.**

517 **(A)** Schematic of *in vivo* fiber photometry and behavior.

518 **(B)** Representative GCaMP6s expression in the BNST and PBN of a vGAT-Cre mouse (scale

519   bars: 100 µm BNST, 200 µm PBN).

520 **(C)** Representative responses of BNST-PBN^{vGAT} terminals during food consumption trials

521   (shaded areas represent periods of eating).

522 **(D and E)** Average z-scored calcium response of BNST-PBN^{vGAT} terminals during consumption

523   of normal chow under sated conditions (n=57 bouts; 7 mice) and averaged activity of 10-

524   seconds pre- compared to post- consumption initiation over the testing period.
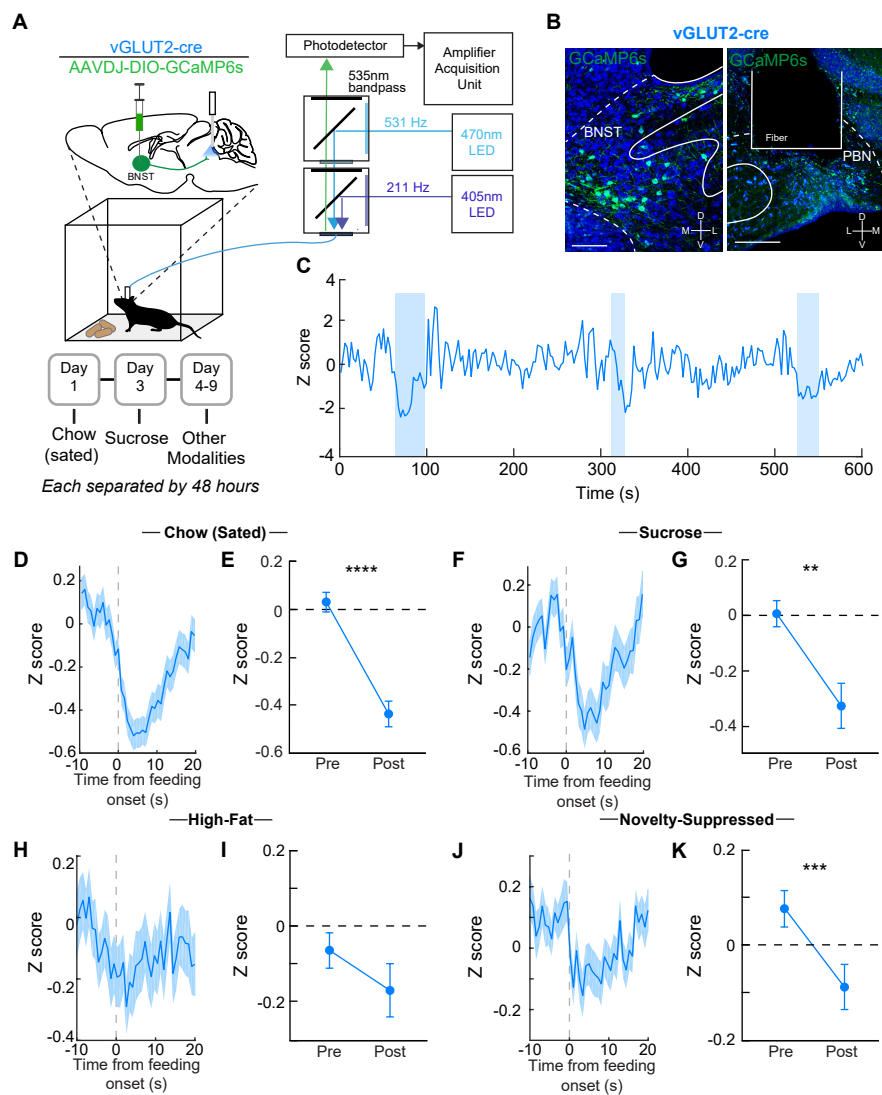
525 **(F and G)** Average z-scored calcium response of BNST-PBN^{vGAT} terminals during consumption

526   of sucrose (n=93 bouts; 7 mice) and averaged activity of 10-seconds pre- compared to post-

527   consumption initiation over the testing period.

528 **(H and I)** Average z-scored calcium response of BNST-PBN^{vGAT} terminals during consumption of

529   high-fat (n=77 bouts; 7 mice) and averaged activity of 10-seconds pre- compared to post-

530   consumption initiation over the testing period.

531 **(J and K)** Average z-scored calcium response of BNST-PBN^{vGAT} terminals during consumption

532   of normal chow under anxiogenic conditions (n=121 bouts; 7 mice) and averaged activity of

533   10-seconds pre- compared to post- consumption initiation over the testing period.

534 **$p < 0.01$, ***$p < 0.001$, ****$p < 0.0001$. Error bars indicate SEM.

535 See also Figure S3.

FIGURE 3

536 **Figure 3. An excitatory BNST-PBN circuit is disengaged during feeding.**

537 **(A)** Schematic of *in vivo* fiber photometry and behavior.

538 **(B)** Representative GCaMP6s expression in the BNST and PBN of a vGLUT2-Cre mouse (scale

539 bars: 100 μm BNST, 200 μm PBN).

540 **(C)** Representative responses of BNST-PBN^{vGGLUT2} terminals during food consumption trials

541 (shaded areas represent periods of eating).

542 **(D and E)** Average z-scored calcium response of BNST-PBN^{vGLUT2} terminals during consumption

543 of normal chow under sated conditions (n=133 bouts; 6 mice) and averaged activity of 10-

544 seconds pre- compared to post- consumption initiation over the testing period.

545 **(F and G)** Average z-scored calcium response of BNST-PBN^{vGLUT2} terminals during consumption

546 of sucrose (n=87 bouts; 6 mice) and averaged activity of 10-seconds pre- compared to post-

547 consumption initiation over the testing period.

548 **(H and I)** Average z-scored calcium response of BNST-PBN^{vGLUT2} terminals during consumption

549 of high-fat (n=56 bouts; 6 mice) and averaged activity of 10-seconds pre- compared to post-

550 consumption initiation over the testing period.

551 **(J and K)** Average z-scored calcium response of BNST-PBN^{vGGLUT2} terminals during consumption

552 of normal chow under anxiogenic conditions (n=77 bouts; 6 mice) and averaged activity of 10-

553 seconds pre- compared to post- consumption initiation over the testing period.

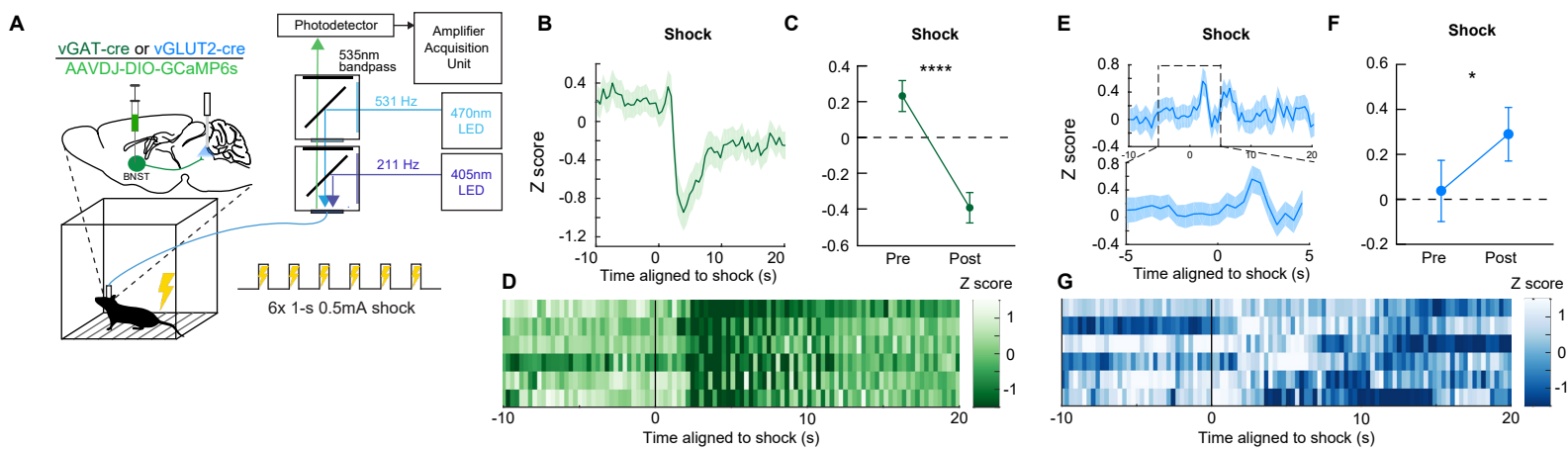554 **$p < 0.01$, ***$p < 0.001$, ****$p < 0.0001$. Error bars indicate SEM.

555 See also Figure S3.

FIGURE 4

556   **Figure 4. Distinct BNST-PBN circuits display opposing responses to aversive stimuli.**

557   **(A)** Schematic of *in vivo* fiber photometry and behavior.

558   **(B)** Average z-scored calcium transient responses of BNST-PBN^{vGAT} terminals to an aversive

559   shock (n=7 mice).

560   **(C)** Mean z-scored calcium transient responses of BNST-PBN^{vGAT} terminals (n=7 mice) 10-

561   seconds before and after the shock initiation.

562   **(D)** Representative heatmap of BNST-PBN^{vGAT} terminal calcium transient activity of a single

563   mouse during aversive shock presentation.

564   **(E)** Average z-scored calcium transient responses of BNST-PBN^{vGLUT2} terminals to an aversive

565   shock (n=6 mice).

566   **(F)** Mean z-scored calcium transient responses of BNST-PBN$^{v\ GLUT2}$ terminals (n=6 mice) 10-

567   seconds before and after the shock initiation.

568   **(G)** Representative heatmap of BNST-PBN^{vGLUT2} terminal calcium transient activity of a single
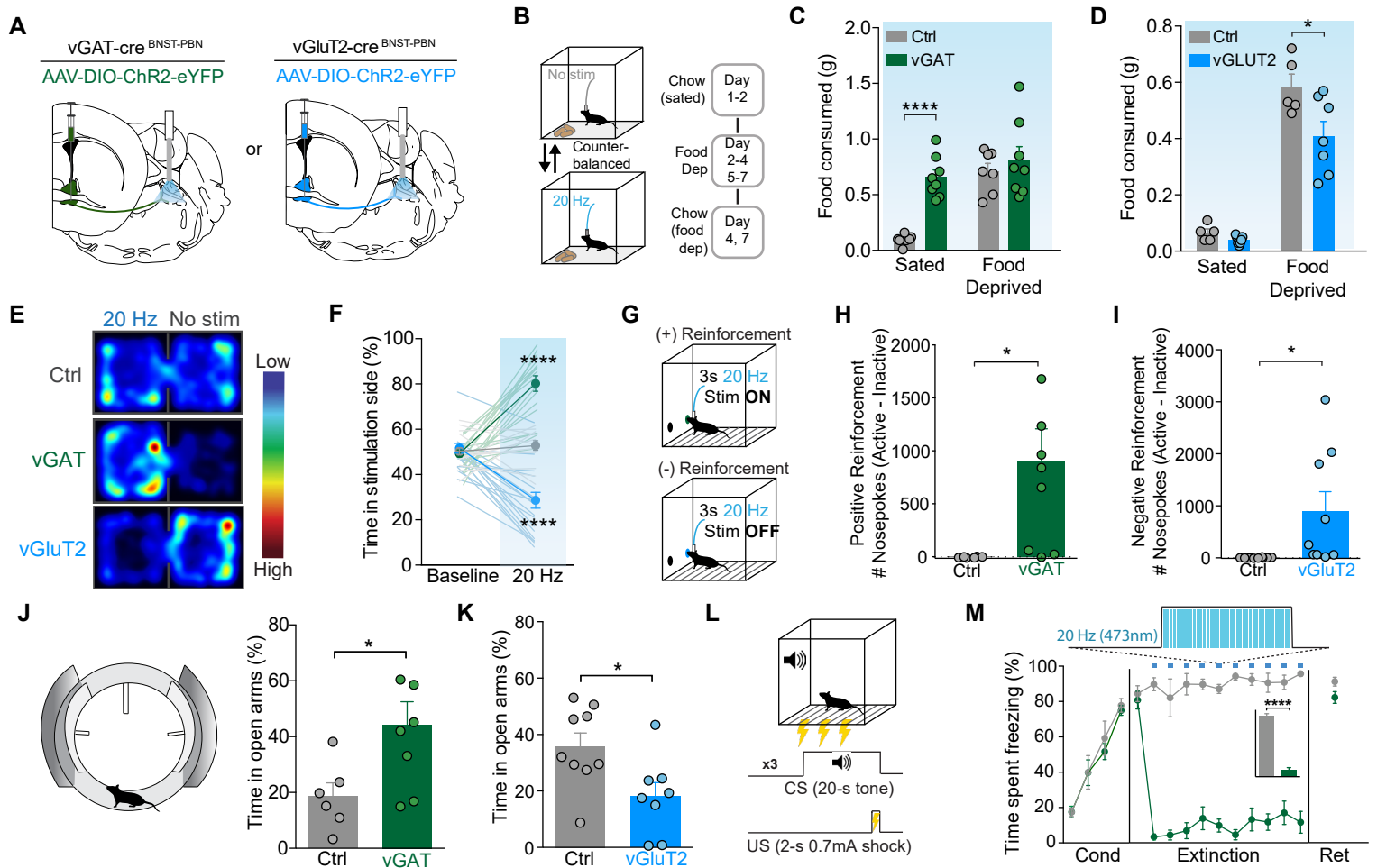
569   mouse during aversive shock presentation.

570   **p < 0.01, ***p < 0.001, ****p < 0.0001. Error bars indicate SEM.

571   See also Figure S3.

FIGURE 5

572 **Figure 5. Distinct BNST-PBN circuits drive opposing feeding and affective behaviors.**

573 **(A)** Schematic of optogenetic approach to target BNST-PBN^{vGAT} and BNST-PBN^{vGLUT2}.

574 **(B)** Schematic of food consumption assay.

575 **(C)** BNST-PBN^{vGAT} activation increases consumption of normal chow under sated conditions

576   (ChR2, $n = 8$; Ctrl, $n = 7$).

577 **(D)** BNST-PBN^{vGLUT2} activation decreases consumption of normal chow after food-deprivation

578   (ChR2, $n = 7$; Ctrl, $n = 5$).

579 **(E)** Representative heatmaps of time spent in the RTPP for Ctrl, BNST-PBN^{vGAT}:ChR2, and

580   BNST-PBN^{vGLUT2}:ChR2 mice.

581 **(F)** BNST-PBN^{vGAT} activation elicits a real-time place preference, while BNST-PBN^{vGLUT2} activation

582   elicits a real-time place aversion compared to control mice (vGAT:ChR2, $n = 18$;

583   vGLUT2:ChR2, n = 18; Ctrl, $n = 25$).

584 **(G)** Schematic of positive (+) and negative (-) reinforcement tasks for assessment in BNST-

585   PBN^{vGAT}:ChR2 and BNST-PBN^{vGLUT2}:ChR2, respectively.

586 **(H)** BNST-PBN^{vGAT} activation is positively reinforcing in an operant-self stimulation task (ChR2, n

587   = 8; Ctrl, $n = 6$).

588 **(I)** BNST-PBN^{vGLUT2} activation is negatively reinforcing in an operant task to turn off optogentic

589   stimulation (ChR2, $n = 8$; Ctrl, $n = 6$).

590 **(J)** BNST-PBN^{vGAT} activation increases time spent in the open arms in the elevated zero maze

591   (ChR2, $n = 8$; Ctrl, $n = 6$).

592 **(K)** BNST-PBN^{vGLUT2} activation decreases time spent in the open arms in the elevated zero maze
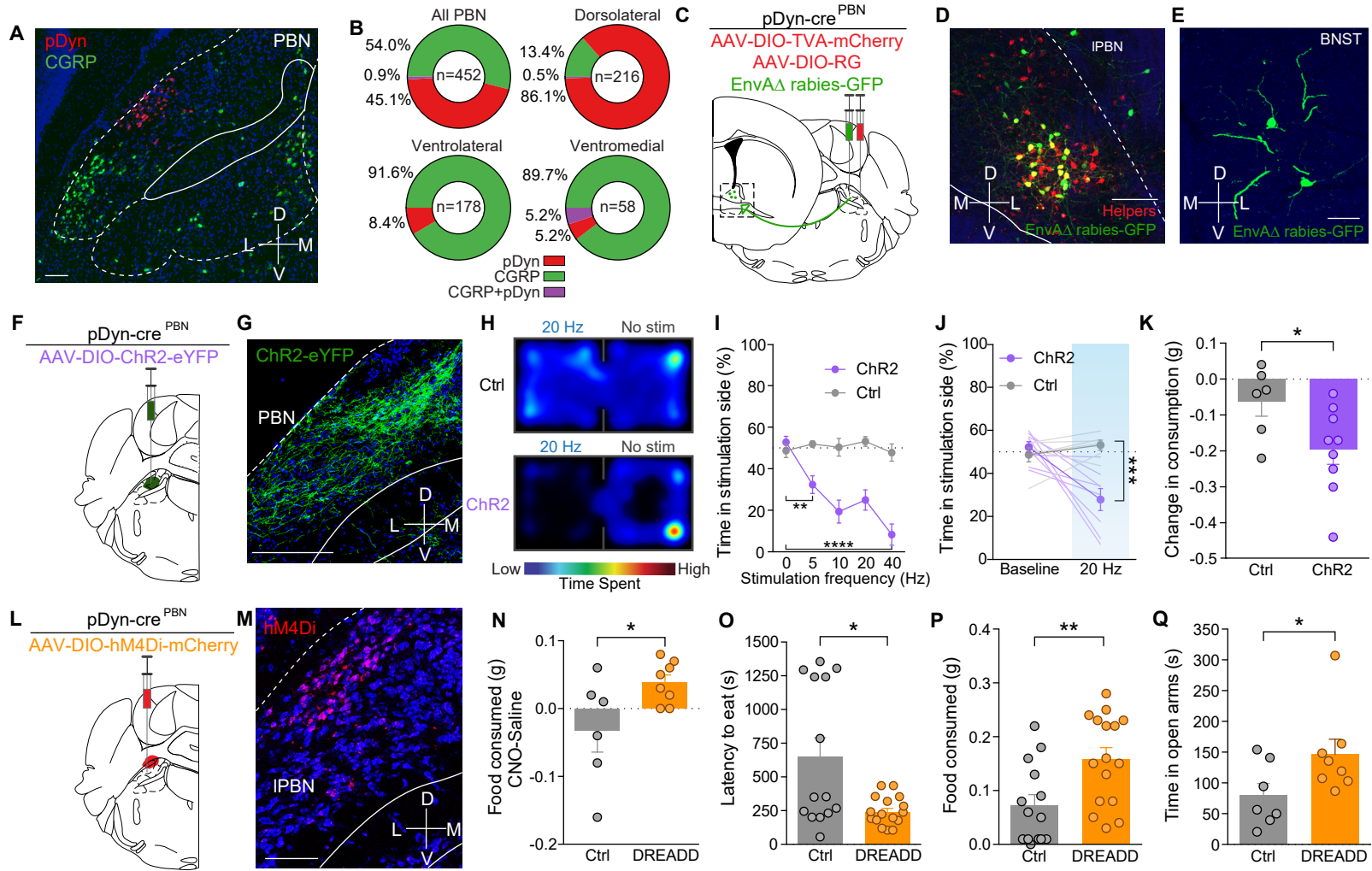
593   (ChR2, $n = 9$; Ctrl, $n = 8$).

594 **(L)** Schematic of the fear conditioning protocol.

595 **(M)** BNST-PBN^{vGAT} activation suppresses cued-defensive responses (i.e. freezing) after

596   conditioning (ChR2, $n = 8$; Ctrl, $n = 6$).

597 *$p < 0.05$, **$p < 0.01$, ***$p < 0.001$, ****$p < 0.0001$. Error bars indicate SEM.

598   See also Figure S4 and S5.

FIGURE 6

599   **Figure 6. Dynorphin-expressing PBN neurons receive BNST input to bidirectionally**

600   **modulate feeding and affective behaviors.**

601   **(A)** Fluorescent *in-situ* hybridization of pDyn and CGRP in the PBN (scale bar: 100μm).

602   **(B)** pDyn and CGRP neurons are genetically and anatomically distinct populations in the PBN

603   (n=452 cells).

604   **(C)** Viral schematic for rabies tracing of monosynaptic inputs to PBN^{pDyn} neurons.

605   **(D)** Starter cells in the PBN expressing TVA-mCherry and rabies-GFP (scale bar: 100 μm).

606   **(E)** and their corresponding input cells in the BNST (scale bar: 50 μm).

607   **(F)** Schematic of optogenetic approach to target PBN^{pDyn} neurons.

608   **(G)** ChR2-eYFP expression in PBN^{pDyn} neurons (scale bar: 200 μm).

609   **(H)** Representative heatmaps of time spent in the RTPP for Ctrl and PBN^{pDyn}:ChR2 mice.

610   **(I and J)** PBN^{pDyn} activation elicits a real-time place aversion in a **(I)** frequency-dependent manner

611   including at **(J)** 20 Hz (ChR2, $n = 8$; Ctrl, $n = 6$).

612   **(K)** PBN^{pDyn} activation decreases food consumption after food-deprivation (ChR2, $n = 8$; Ctrl, $n =$

613   6).

614   **(L)** Schematic of chemogenetic approach to target PBN^{pDyn} neurons.

615   **(K)** hM4Di -mCherry expression in PBN^{pDyn} neurons (scale bar: 100μm).

616   **(N-Q)** Chemogenetic inhibition of PBN^{pDyn} neuron increases **(N)** food consumption, **(O)** decreases

617   latency to eat and **(P)** while increasing food consumed in a novelty-suppressed feeding task

618   and **(Q)** time spent in the open arms of elevated zero maze (DREADD, $n = 7$-8; Ctrl, $n = 6$-7).

619   *$p < 0.05$, **$p < 0.01$, ***$p < 0.001$, ****$p < 0.0001$. Error bars indicate SEM.

620   See also Figure S6.

1 **Methods**

2 **Key Resources Table**
3

REAGENT or RESOURCE	SOURCE	IDENTIFIER
Antibodies		
Bacterial and Virus Strains		
retroAAV2-EF1a-DIO-hChR2-(H134R)-eYFP	WashU HOPE Center Viral Core	N/A
AAV5-EF1a-DIO-hChR2-(H134R)-eYFP	WashU HOPE Center Viral Core	N/A
retroAAV2-231-TRAP-Cre-On	WashU HOPE Center Viral Core	N/A
AAV-DJ-EF1a-DIO-GCaMP6s	Stanford University Gene Vector and Viral Core	N/A
AAV5-EF1a-DIO-Arch3.0-eYFP	UNC Vector Core	N/A
AAV5-Ef1a-DIO-hM4D(Gi)-mCherry	UNC Vector Core	N/A
AAV5-CAG-FLEX-RG	UNC Vector Core	N/A
AAV8-EF1a-FLEX-TVA-mCherry	UNC Vector Core	N/A
EnvA-G-Deleted Rabies-eGFP	Salk	N/A
Chemicals, Peptides, and Recombinant Proteins		
Clozapine-N-Oxide (CNO)	Sigma-Aldrich	Cat#C0832
NeuroTrace 435/455 Blue Fluorescent Nissl Stain	ThermoFisher Scientific	Cat# N21479
VECTASHIELD Hardset Antifade Mounting Medium	Vector Laboratories	Cat#H-1400
Critical Commercial Assays		
RNAscope Fluorescent Multiplex Kit 2.0	Advanced Cell Diagnostics	Cat#320850
Wash Buffer Reagents	Advanced Cell Diagnostics	Cat#310091
Protease III & IV Reagents	Advanced Cell Diagnostics	Cat#322340
CGRP (*Calca*)	Advanced Cell Diagnostics	*Cat#420361*
Pdyn	Advanced Cell Diagnostics	*Cat#318771*
vGAT (*Slc32a1*)	Advanced Cell Diagnostics	*Cat#319191*
vGLUT2 (*Slc17a6*)	Advanced Cell Diagnostics	*Cat#319171*
eGFP	Advanced Cell Diagnostics	*Cat#400281*

Adcyap1	Advanced Cell Diagnostics	*Cat#405911*
Sstr3	Advanced Cell Diagnostics	*Cat#460621*
Tac2	Advanced Cell Diagnostics	*Cat#446391*
Calcr	Advanced Cell Diagnostics	*Cat#*494071
Deposited Data		
RNA sequencing	GEO	GSE133484
Experimental Models: Organisms/Strains		
Mouse: vGAT-IRES-Cre (*Slc32a1*$^{tm2(cre)Lowl}$/J)	The Jackson Laboratory	Stock #016962
Mouse: vGLUT2-IRES-Cre (*Slc17a6*$^{tm2(cre)Lowl)}$/J)	The Jackson Laboratory	Stock # 016963
Mouse: *Pdyn*$^{tm1.1(cre)Mjkr}$/J	The Jackson Laboratory	Stock #027958
Software and Algorithms		
Image processing, cell counter module	ImageJ/Fiji	https://imagej.net/Fiji
Graphpad Prism 6.0 and 8.0	GraphPad Software	https://www.graphpad.com/scientificsoftware/prism/
Illustrator CS6	Adobe	https://www.adobe.com/products/illustrator.html
EthoVision XT 10	Noldus	https://www.noldus.com/animal-behavior-research/products/ethovision-xt
MATLAB	MathWorks	https://www.mathworks.com/
pClamp 10 (Clampfit,Clampex)	Molecular Devices	https://www.moleculardevices.com/systems/conventional-patch-clamp/pclamp-10-software
R	R Foundation for Statistical Computing	https://www,r-project.org
Leica LAS X	Leica Microsystems	https://www.leica-microsystems.com/products/microscope-software/p/leica-las-x-ls/

Med-PC V Software Suite	Med-Associates, Inc.	https://www.med-associates.com/med-pc-v/
STAR	Doblin et al., 2013	https://code-google-com.ezp-prod1.hul.harvard.edu/archive/p/rna-star/

Contact for Reagent and Resource Sharing

Further information and requests for resources and reagents should be directed to and will be fulfilled by the Lead Contact, Dr. Michael Bruchas (mbruchas@uw.edu).

Experimental Model and Subject Details

Animals

Adult male vGAT-IRES-Cre (*Slc32a1$^{tm2(cre)Lowl}$*/J; Jackson Laboratory #016962) (Vong et al., 2011), vGLUT2-IRES-Cre (*Slc17a6$^{tm2(cre)Lowl)}$*/J; Jackson Laboratory # 016963), and preprodynorphin(*Pdyn*)-IRES-Cre (*Pdyn$^{tm1.1(cre)Mjkr}$*/J; Jackson Laboratory #027958) (Krashes et al., 2014) mice were group housed, given access to food and water *ad libitum*, and maintained on a 12:12 hr light:dark cycle (lights on at 7:00 AM). All animals were kept in an isolated and sound-attenuated holding facility within the lab and adjacent to behavior rooms one week prior to surgery, post-surgery, and throughout the duration of the behavioral assays to minimize stress. All procedures were approved by the Animal Care and Use Committee of Washington University and the University of Washington and conformed to US National Institutes of Health guidelines.

Method Details

Stereotaxic Surgeries

After the animals were acclimated to the holding facility for at least seven days, the mice were anaesthetized in an induction chamber (2% isoflurane) and placed into a stereotaxic frame (Kopf Instruments, Model 1900) where they were maintained at 1-2% isoflurane. Mice were then injected using a blunt needle (86200, Hamilton) at a rate of 100 nL/min with 300-400 nL in the BNST (AP +0.14, ML ±0.9, DV -4.5) or PBN (AP -5.3, ML ±1.1, DV -3.5); unilateral for optogenetic activation, tracing, and fiber photometry experiments; bilateral for optogenetic or chemogenetic experiments. Needle was slowly removed from the brain 10 min after cessation of injection to allow for diffusion. For fiber photometry experiments, mice were also implanted with a 400-μm fiber optic (Doric Inc., MFC_400/430-0.48_MF2.5_FLT) in the same surgery. Mice recovered for at least 6 weeks prior to behavioral testing, permitting optimal expression of the virus. For optogenetic activation and fiber photometry experiments, five weeks after viral injection, intracranial optic fiber implants were directed above the PBN unilaterally (AP -5.3, ML ± 1.1, DV -3.0). For optogentic inhibition inhibition, fiber optics were placed bilaterally. The fiber optic implants were secured using two bone screws (CMA, 743102) and affixed with TitanBond (Horizon Dental Products) and dental cement (Lang Dental).

Immunohistochemistry

45 Immunohistochemistry was performed as previously described (McCall et al., 2017). In brief, mice
46 were anesthetized with sodium pentobarbital and transcardially perfused with 4%
47 paraformaldehyde (PFA), post-fixed overnight in 4% PFA, and cryo-protected in 30% sucrose for
48 at least 24 hours. Brains were then sectioned (30 µm) and placed in 0.1M PB until
49 immunohistochemistry. Free-floating sections were washed in 0.1M PBS for 3 x 10 minutes
50 intervals. Sections were then placed in blocking buffer (0.5% Triton X-100 and 5% natural goat
51 serum in 0.1 M PBS) for 1 hr at room temperature. After blocking buffer, sections were incubated
52 in NeuroTrace (1:400, 435/455 blue fluorescent Nissl stain, Invitrogen #N21479) for 1 hour,
53 followed by 3 x 10 minute 0.1 MPBS then 3 x 10 minute 0.1 M PB washes. After immunostaining,
54 sections were mounted and coverslipped with Vectashield HardSet mounting medium (Vector
55 Laboratories) and imaged on a Leica TCS SPE confocal microscope. Animals that did not show
56 targeted expression were excluded.
57
58 **Fluorescent In-Situ Hybridization (FISH)**
59
60 Animals were anesthetized and rapidly decapitated. Brains were quickly removed and fresh
61 frozen in dry ice, then stored at -80°C. Sections were cut at 20µm, mounted on slides, and stored
62 at -80°C. Sections were fixed in 4% PFA for 15 min, dehydrated in serial ethanol concentrations
63 (50%, 70%, and 100%) and processed with RNAscope (Advanced Cell Diagnostics, cat. No.
64 320293). Sections were hybridized with the probes listed below. Sections were then
65 counterstained with DAPI and coverslipped. Confocal images were obtained on an Olympus
66 FV3000RS microscope. Circular ROIs were drawn around each cell, and these ROIs were then
67 used for co-expression analysis.
68
69 **Slice Electrophysiology**
70
71 Acute brain slices were prepared using a protective cutting and recovery method (Ting et al.,
72 2014). Anesthetized mice infected with AAV5-EF1a-DIO-hChR2-(H134R)-eYFP were
73 transcadially perfused with NMDG-substituted aCSF containing (in mM) 93 NMDG, 2.5 KCl, 1.25
74 NaH2PO4, 30 NaHCO3, 20 HEPES, 25 glucose, 5 ascorbic acid, 2 thiourea, 3 Na-pyruvate, 12
75 N-acetyl-L-cysteine, 10 MgSO4, 0.5 CaCl2 (pH = 7.3-7.4). 200 mm thick coronal sections of the
76 PBN were cut using a Vibratome VT1000s (Leica) and transferred to an oxygenated recovery
77 chamber containing NMDG aCSF for 5–10 min at 32°C –34°C before being transferred to a
78 holding chamber filled with modified aCSF containing (in mM) 92 NaCl, 2.5 KCl, 1.2 NaH2PO4,
79 30 NaHCO3, 20 HEPES, 25 glucose, 2 CaCl2, 2 MgCl2 (pH adjusted to 7.3-7.4 with NaOH), and
80 Osm 290-310. Whole-cell patch-clamp recordings were made using fire-polished glass pipettes
81 with a resistance of 3-5 MΩ filled with (in mM): 120 K+ gluconate, 5 NaCl, 2 MgCl2, 0.1 CaCl2,
82 10 HEPES, 1.1 EGTA, 4 Na2ATP, 0.4 Na2GTP, 15 phosphocreatine; pH adjusted to 7.3 with
83 KOH, 291 mOsm. BNST axonal projections in the PBN were visualized through a 40x objective
84 using IR-DIC microscopy on an Olympus BX51 microscope, and neurons with YFP+ axons in
85 close proximity were identified using epifluorescent illumination. Recordings were made with
86 Patchmaster software controlling a HEKA EPC10 amplifier. Following gigaseal formation and
87 stable whole-cell access, currents elicited by 10 ms-pulse stimulation of ChR2-containing axonal
88 terminals and isolated by blocking AMPA/KARs (10 µM NBQX, Abcam), NMDARs (50 µM D-APV,
89 Abcam), GABAARs (100 µM picrotoxin and 50 µM bicuculline, Abcam) through bath application
90 of the antagonists in aCSF solution. Neurons were voltage clamped at -70 mV for eEPSCs and 0
91 mV for eIPSCs. Input resistance was monitored to maintain cells with a stable Rs < 35 MΩ, and
92 only these neurons were included in our analysis. eIPSC and eEPSC amplitudes were averaged
93 across 5 sweeps per cell.
94
95 **Translating Ribosome Affinity Purification (TRAP)**

96

97   In order to specifically capture transcribed RNA from GABAergic and glutamatergic
98 neurons synapsing on the PBN, we generated an adenoviral vector encoding a floxed fusion GFP-
99 ribosomal protein (RPL10A), and packaged it into the retrofecting AAV serotype rAAV2-retro
100 (Tervo et al., 2016). This design restricts expression of the GFP•RPL10A fusion to a target (Cre-
101 expressing) cell type, and further restricts expression to cells of that type synapsing onto the
102 transduced region.

103   In order to selectively capture transcripts from those excitatory and inhibitory neurons in
104 the BNST synapsing onto the PBN, we delivered the floxed eGFP•Rpl10a retro-AAV2 into the
105 PBN of adult male mice ages 4m-10m expressing Cre recombinase under a glutamatergic
106 (vGLUT2) or GABAergic (vGAT) neuron-specific promoter. At least 6 weeks were given for
107 surgical recovery and transgene expression before mice were sacrificed for brain dissection,
108 homogenization, and GFP-targeted immunoprecipitation.

109   In order to control for stress and circadian effects on BNST transcripts between replicates,
110 mice to be sacrificed were always retrieved between 10AM and 12PM immediately before deep
111 anesthetization by isoflurane, followed by rapid removal of the brain. A 1mm coronal slab of brain
112 tissue was collected from AP ±0.5 mm, ML ±1.2mm, DV -3.8 to -4.8mm and microdissected in ice
113 cold PBS containing RNAse inhibitors (rRNAsin, Superasin), 500 μM DTT, and cycloheximide (to
114 arrest translation in progress to keep ribosomes associated with their RNAs for later capture).
115 Three dissected BNSTs were pooled per replicate in order to minimize effects of dissection and
116 incidental injection of structures adjacent to PBN. Pooled tissue was homogenized and processed
117 using the standard TRAP protocol as previously described (Rieger et al., 2018). All RNA samples
118 were quality checked for RINe (estimated RNA integrity number) on an Agilent Tapestation 4200
119 (Agilent Technologies, Santa Clara, California) using the High-Sensitivity RNA Assay Kit. All
120 sequenced samples had a RINe of > 7.5 with total mass yielded per sample ranging from 2.5 ng
121 to 250ng.

122   RNA samples were submitted to Washington University in St Louis' Genome Technology
123 Access Center for library preparation and mRNA sequencing. cDNAs were synthesized using
124 polyA capture (Dynal mRNA Direct Kit, Life Technologies, Carlsbad, California). cDNAs were
125 synthesized by polyA-targeted priming, followed by cDNA amplification using the Clontech
126 SMARTer kit (Takara Bio, Mountain View, CA).

127   Single-read, 50bp RNA-seq of IP fractions and total homogenate from 5 replicates per cell
128 type (20 samples total) was performed on a single lane of a HiSeq 3000 (Illumina, San Diego,
129 California), yielding ~350M reads, ranging from 10M to 25M per sample. Reads were processed
130 using a standard pipeline of read trimming with Trimmomatic (Bolger et al., 2014), removal of
131 rRNA reads using BowTie (Langmead et al., 2009), and alignment to mouse genome build 38.p5
132 along with gene-level feature counts using STAR aligner (Dobin et al., 2013).

133   Samplewise read counts were first subsetted to those reads with a normal distribution in
134 order to perform downstream differential expression analysis, as recommended for analyses in
135 EdgeR(McCarthy et al., 2012; Robinson et al., 2010). Gene counts were then quality-checked by
136 hierarchical clustering to rule out batch effects and off-target cell enrichment. One replicate
137 clustered separately from all other samples and was excluded. Additional quality checks included
138 plotting relative enrichment / depletion of vGAT/vGLUT2-specific marker genes and that of off-
139 target cell types (e.g. astrocytes and oligodendrocytes). Ultimately, 3 replicates for vGLUT2
140 neurons and 2 replicates for vGAT neurons were used for analysis.

141   Differential expression analysis was performed in EdgeR using the following model for
142 single-cell type enriched transcripts, where group was vGLUT2 IP, vGLUT2 input, vGAT IP, or
143 vGAT input:

144   Expression ~ 0+group

145   Enrichment in cell types was then determined using EdgeR's glmQLFtest function using
146 contrasts of vGLUT2 Enriched = (vGLUT2 IP) – (vGLUT2 Input) and likewise for vGAT.

147　　　　　Differential expression analysis between cell types was performed using the same model
148　as above but with a contrast of (vGLUT2-vGAT Differential Expression) = (vGLUT2 IP – vGLUT2
149　Input) – (vGAT IP – vGAT Input). This contrast thus regresses potential effects of dissection
150　heterogeneity before comparing the target immunoprecipitated cell types. The supplementary
151　data (**Table S2-S5**) contains differential expression results for all of the contrasts described
152　above, as well as an additional contrast between immunopreciptates for vGLUT2 and vGAT
153　without normalizing for input RNAs (that is, vGLUT2-vGAT differential expression, alternate
154　calculation = vGLUT2 IP – vGAT IP). Raw data can be found in the NCBI Gene Expression
155　Omnibus (GEO) database (GSE133484).
156
157　**Behavior**
158
159　Behavioral assays were performed in sound attenuated rooms maintained at 23°C. Lighting was
160　measured and stabilized at ~100 lux for anxiety testing in vGAT-Cre experiments, ~20 lux for
161　anxiety testing in vGlut-Cre experiments, and ~200 lux for place testing. All behavioral
162　apparatuses were cleaned with 70% ethanol in between animals. Movements were video
163　recorded and analyzed using Ethovision Software or recorded with Media Recorder.
164
165　*Real-Time Place Preference (RTPP)*
166　Mice were placed into a custom-made unbiased, balanced two-compartment conditioning
167　apparatus (52.5 x 25.5 x 25.5 cm) as previously described (McCall et al., 2017) and allowed to
168　freely roam the entire apparatus for 30 min. Entry into one compartment triggered constant
169　photostimulation (0-40 Hz; 5-10 mW light power) while the animal remained in the light-paired
170　chamber. Entry into the other chamber ended the photostimulation. The side paired with
171　photostimulation was counterbalanced across mice. Time spent in each chamber and total
172　distance traveled for the entire 30 min trial was measured using Ethovision 8.5 (Noldus). Data are
173　expressed as mean +/- S.E.M percent time spent in photostimulation-paired chamber.
174
175　*Operant Conditioning: Positive Reinforcement*
176　For positive reinforcement induced by vGAT-containing BNST-PBN projections, mice with optical
177　fibres implanted above the PBN were trained in one 1-hr session to nose poke on a fixed-ratio 1
178　schedule for optical self-stimulation (3-s, 20-Hz. ~10 mW, 473nm) in a mouse operant chamber
179　(17.8 x 15.2 x 18.4 cm; Med Associates) (Jennings et al., 2013). The following day, the mice were
180　run again with the same conditions and the number of nosepokes recorded in the hour session
181　was recorded.
182
183　*Operant Conditioning: Negative Reinforcement*
184　For negative reinforcement induced by vGLUT2-containing BNST-PBN projections, mice with
185　optical fibres implanted above the PBN were trained in one 1-hr session to nose poke on a fixed-
186　ratio 1 schedule to turn off optical self-stimulation in a mouse operant chamber (17.8 x 15.2 x 18.4
187　cm; Med Associates). Constant photostimulation (20-Hz, ~10 mW, 473nm) began at the start of
188　each session. Each nose poke resulted in the cessation of the photostimulation for 3-s. The
189　following day, the mice were run again with the same conditions. The number of nosepokes
190　recorded in the hour session was recorded. About 50% of Cre+ mice did not learn the operant
191　task and thus were excluded from the results as non-responders (**Fig. S7F**). Non-responders
192　were classified as animals whose difference of responses between active and inactive was < 5.
193
194　*Threat Conditioning*
195　　　　　Pavlovian threat conditioning was performed in Med Associates Fear Conditioning
196　Chambers (NIR-022MD). This equipment consisted of a conductive grid floor inside a 29.53 cm
197　L x 23.5 cm W x 20.96 cm H chamber inside of a soundproof box lit by an infrared light.

198   vGAT-Cre experiments: Mice were conditioned to four 20s tones co-terminating with 2-s
199   0.7mA shocks on Day 1. On Day 2, mice were placed back into the chamber. Eleven tone
200   presentations in the absence of shock were presented. During the first tone, no optostimulation
201   occurred. During the next ten tone presentations, 20 Hz blue light was delivered. On the third day,
202   we assessed extinction recall by placing the mice into the chamber and presented the tone once.
203   Freezing behavior was measured during all tone presentations.
204   All fiber photometry animals were conditioned to 6 20-second tones terminating with a 1-
205   s 0.5mA shock.
206
207   *Feeding Assays*
208   Feeding assays were performed in a square plexiglass arena (27 cm × 27 cm). Chow,
209   High-fat, sucrose, or salt pellets (Envigo) were placed in the corner of the arena. Mice were then
210   introduced into the arena for 30 min. To record the amount of food consumed, pellets were
211   measured before and after the assay. Baseline feeding and feeding whilst photostimulation (20
212   Hz; 5-10 mW light power) or photoinhibition (constant; ~5 mW light power) were performed in a
213   counterbalanced fashion across mice.
214   In addition to counterbalanced experiments across days, we also performed within-
215   session manipulations to assess whether the effects are immediately reversible. Mice were
216   introduced into the arena for 60 minutes: 20 min pre-stimulation, 20 min 20 Hz stimulation or
217   constant inhibition, and 20 min post-stimulation. Food weight was measured at each 20 min point
218   (**Fig. S5J, S7E, S8E**).
219
220   *Elevated Zero Maze*
221   EZM testing was performed as described previously (McCall et al., 2017) , the EZM
222   (Harvard Apparatus) was made of grey plastic, 200 cm in circumference, comprised of four 50 cm
223   sections (two opened and two closed). The maze was elevated 50 cm above the floor and had a
224   path width of 4 cm with a 0.5 cm lip on each open section. Mice were connected to fiber optic
225   cables, positioned head first into a closed arm, and allowed to roam freely for 7 min. Animals
226   received 20 Hz (10 ms pulse width) photostimulation (5-10 mW light power). Open arm time was
227   the primary measure of anxiety-like behavior.
228
229   **Fiber Photometry**
230
231   Fiber photometry recordings were performed as previously described (Parker et al., 2019).
232   Briefly, an optic fiber was attached to the implanted fiber by a ferrule sleeve, then GCaMP6s was
233   stimulated by two LEDs, a 531-Hz sinusoidal light (Thorlabs M470F3), bandpass filtered at 470 ±
234   20nm, and a 211-Hz sinusoidal light (Thorlabs M405FP1), bandpass filtered at 405 ± 10nm. (Filter
235   cube: Doric FMC4; LED driver: DC4104). The 470 nm signal evokes Ca^{2+}-dependent emission,
236   while the 405 nm signal evokes Ca^{2+}-independent isobestic control emission. Prior to recording,
237   a 180s period of GCaMP6s excitation with both light channels was used to remove the majority
238   of baseline drift. Laser intensity at the optic fiber tip was adjusted to ~50 µW before each day of
239   recording. GCaMP6s fluorescent signal was isolated by bandpass filtering (525 ± 25nm),
240   transduced by a femtowatt silicon photoreceiver (Newport 2151), and recorded by a real-time
241   processor (TDT RZ5P). The envelopes of 531 Hz and 211 Hz signals were extracted in real time
242   by the TDT program Synapse at a sampling rate of 1017.25 Hz.
243   Fiber recordings were analyzed using custom MATLAB scripts available on Github. Motion
244   artifacts were removed by subtracting the isobestic 405 nm signal from the 470 nm excitation
245   signal. Baseline drift due to slow photobleaching artifacts was corrected by fitting a double
246   exponential curve to the raw trace, then the photometry trace was z-scored relative to the mean
247   and standard deviation of the signal. The mean z-score during the ten seconds preceding and
248   following an event were compared using paired t tests.

Statistical analyses

All summary data are expressed as mean ± SEM. Statistical significance was taken as *p < 0.05, **p < 0.01, ***p < 0.001, ****p < 0.0001, as determined by the Student's t-test (paired and unpaired): One-Way Analysis of Variance (ANOVA) or One-Way Repeated Measures ANOVA, followed by Bonferroni post hoc tests as appropriate. Statistical analyses were performed in GraphPad Prism 6.0 or 8.0. All statistical information is listed in **Table S1.**

Data and Code Availability

RNA sequencing data from Figure 1 have been deposited and are available from GEO (Accession: GSE133484). Custom MATLAB analysis code was created to appropriately organize, process, and combine photometry recording data with associated behavioral data. Analysis code for photometry from Figures 2, 3, and 4 is available online at https://www.github.com/BruchasLab. The full behavioral dataset supporting the current study are available from the corresponding author upon request.